RJES Russian Journal of Earth Sciences Online ISSN: 1681-1208

Analysis of Crustal Deformations Associated with Major Chilean Earthquakes of the Early 21st Century Using GNSS Observations

N. S. Shcheveva[1] and I. S. Vladimirova[1,2,*]

[1]Shirshov Institute of Oceanology of Russian Academy of Sciences, Moscow, Russian Federation
[2]Institute of Earthquake Prediction Theory and Mathematical Geophysics of Russian Academy of Sciences, Moscow, Russian Federation
* **Correspondence to:** Irina Vladimirova, vladimirova.is@ocean.ru

Abstract: This study presents an analysis of the surface deformations along the Chilean coastline before and after a series of major earthquakes in the early 21st century. The planar strain-rate field was computed using Shen's method applied to continuous GNSS observations from Chile and Argentina. Results reveal an increase in strain rates proximal to the earthquake sources during the preseismic period. Conversely, the postseismic period is characterized by a reduction in strain rates in the immediate vicinity of the rupture zones, indicative of progressive relaxation of accumulated crustal stresses. The earthquake sources are localized near regions exhibiting pronounced gradients in deformation-related field parameters, underscoring their association with zones of significant stress accumulation and redistribution within the crust.

Keywords: Peru–Chile subduction zone, major earthquakes, surface deformations, satellite geodesy, Shen method, regional faults

Citation: Shcheveva N. S. and Vladimirova I. S. (2026), Analysis of Crustal Deformations Associated with Major Chilean Earthquakes of the Early 21st Century Using GNSS Observations, *Russian Journal of Earth Sciences*, 26, ES3007, EDN: NMRACJ, https://doi.org/10.2205/2026es001091

Review

Received: September 2, 2025
Accepted: November 25, 2025
Published: August 5, 2026

1. Introduction

Chile is located along one of the most seismically active plate boundaries in the world (Figure 1a) – the Peru–Chile subduction zone where the Nazca Plate subducts beneath the South American Plate at a convergence rate of approximately 66–80 mm/yr [*Kendrick et al.*, 2003]. The active subduction process results in frequent strong earthquakes (Figure 1b), high volcanic activity and significant crustal deformation along the Andean margin.

The early 21st century has been marked by a pronounced phase of seismic activation along the central and northern segments of the Peru–Chile subduction zone, characterized by the occurrence of several large-magnitude megathrust earthquakes. Between 2010, 2015, Chile experienced a sequence of major seismic events, including the 2010 Maule earthquake (M_W 8.8), the 2014 Iquique earthquake (M_W 8.1) and the 2015 Illapel earthquake (M_W 8.3).

The Maule earthquake (M_W 8.8) occurred on February 27, 2010 and within a seismic gap that had remained unruptured since the 1835 Concepción earthquake [*Ruiz and Madariaga*, 2018]. This event ruptured ~500–600 km of the plate interface in Central Chile between ~ 35°S and 38.5°S. The earthquake rupture propagated bilaterally, with significant slip (up to 10–12 meters) concentrated near the shallow portion of the subduction zone [*Lin et al.*, 2013; *Moreno et al.*, 2010]. Horizontal displacements of the Earth's surface observed by satellite methods exceeded 3 meters in the near field [*Vladimirova*, 2022]. As one of the largest instrumentally recorded megathrust earthquakes, the 2010 Maule event has been the subject of comprehensive investigations into its coseismic rupture dynamics and subsequent postseismic deformation processes [*Lin et al.*, 2013; *Mikhailov et al.*, 2020; *Mora-Stock and Rabbel*, 2012; *Moreno et al.*, 2010; *Vladimirova et al.*, 2025].

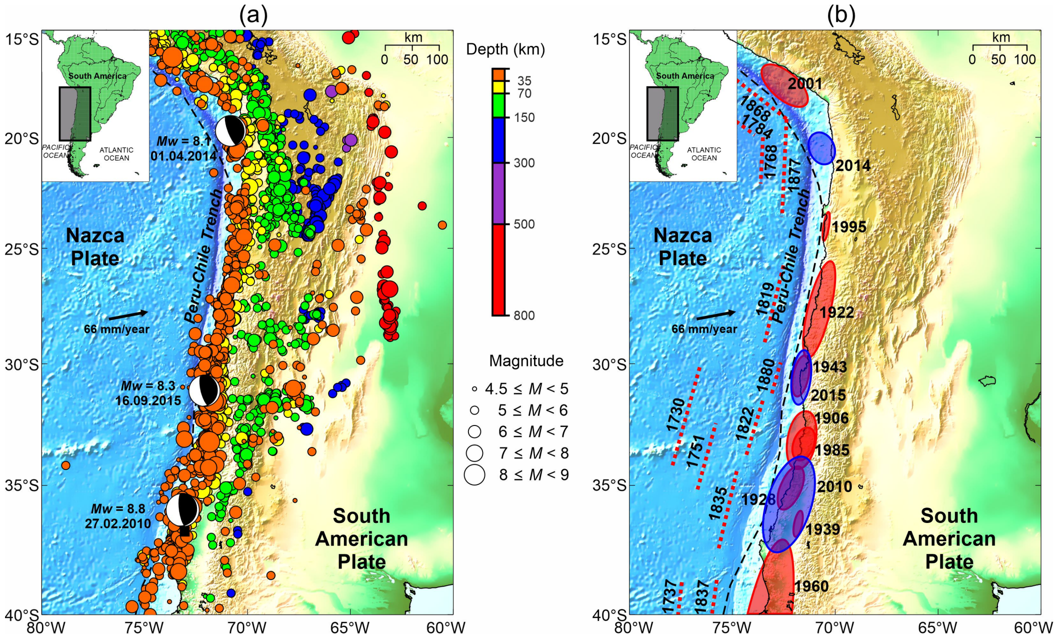

Figure 1. (a) Seismicity of Northern and Central Chile. Epicenters of earthquakes with moment magnitude $M_W \geq 4.5$ from the Global CMT catalog [*Dziewonski et al.*, 1981; *Ekström et al.*, 2012] for the period 1976–2022 are shown as circles. The color scale represents the depth distribution of the hypocenters. Focal mechanisms for the 2010 Maule, 2014 Iquique, and 2015 Illapel earthquakes are also derived from the Global CMT catalog. (b) Fault zones of the major earthquakes in Northern and Central Chile. Rupture zones for the 2010 Maule, 2014 Iquique, and 2015 Illapel events are highlighted in blue. Dashed red lines indicate the estimated rupture extents of great historical earthquakes, based on data from [*Beck et al.*, 1998; *Mora-Stock and Rabbel*, 2012; *Ruiz and Madariaga*, 2018].

The Iquique earthquake (M_W 8.1) occurred on April 1, 2014 in northern Chile, within a region previously identified as a seismic gap that had not ruptured since 1877. This event ruptured a ~150 km portion of the megathrust interface at ~ 19.5°S–21°S. Satellite-based geodetic measurements detected horizontal ground displacements of up to approximately 1 meter associated with this earthquake [*Vladimirova*, 2022]. The event exhibited complex rupture behavior characterized by a slow nucleation phase and heterogeneous slip distribution with maximum displacements reaching 6 meters [*Lay et al.*, 2014; *Vladimirova et al.*, 2025]. Despite its large magnitude, the rupture did not fully release the accumulated seismic potential in the northern Chile subduction zone, leaving adjacent segments still capable of generating future large earthquakes [*Ruiz et al.*, 2014].

The Illapel earthquake (M_W 8.3) occurred on September 16, 2015 along the central-northern Chilean subduction zone. This event ruptured a ~200 km portion of the megathrust between approximately 30°S and 32°S. The Illapel event reactivated a segment of the subduction interface that last ruptured during the 1943 $M_W \sim 7.9$ earthquake. The earthquake rupture involved significant (up to 6–7 meters) slip on the shallow portion of the megathrust [*Easton et al.*, 2022; *Heidarzadeh et al.*, 2016], suggesting high interplate coupling in this area [*Métois et al.*, 2016]. Coseismic displacements measured by satellite geodetic methods exceeded 2 meters near the rupture zone [*Vladimirova*, 2022].

The Maule, Iquique and Illapel earthquakes were accompanied by significant aftershock sequences and widespread coseismic and postseismic deformations. These events have been extensively monitored using dense networks of continuous Global Navigation Satellite System (GNSS) stations, seismic arrays, and satellite-based geodesy (Interferometric Synthetic Aperture Radar – InSAR and GRACE systems), providing detailed observations of coseismic and postseismic deformation. It should be noted that prior to the 2010 Maule earthquake (M_W 8.8), Chile had a limited number of permanent GNSS stations, mostly installed for scientific research and not fully integrated into a national hazard monitoring system. The 2010 Maule earthquake (M_W 8.8) triggered a significant enhancement of geodynamic observation infrastructure along the Chilean margin, aimed at improving the resolution of crustal deformation monitoring in this seismically active zone.

GNSS is an essential geodetic tool for studying various geodynamic processes with high temporal and spatial resolution. In particular, GNSS high-precision measurements provide a reliable basis for quantifying planar strain-rate fields in tectonically active regions. These strain-rate fields are essential for identifying zones of interseismic strain accumulation, characterizing postseismic relaxation following large earthquakes, and detecting transient deformation phenomena such as aseismic creep or slow slip events.

The objective of this study is to analyze the spatiotemporal variations in surface deformation throughout different phases of the seismic cycle within the Peru–Chile subduction zone, based on continuous GNSS observations. Particular attention is given to the identification of anomalous deformation patterns associated with the preparatory phase of major earthquakes and the subsequent postseismic processes.

2. Data and Methods

To investigate the spatiotemporal variations of surface deformations associated with the seismogenic activation of the Chilean subduction zone in the early 21st century, three-component time series from 134 continuous GNSS stations located along the Chilean coast were analyzed. This dataset, spanning the period from 2009 to 2017, was obtained from the Nevada Geodetic Laboratory [*Blewitt et al.*, 2018].

Accurate estimation of GNSS station displacement velocities is critical for constructing robust crustal strain-rate fields. Regression analysis of GNSS time series facilitates the decomposition of station displacements into components associated with distinct deformation processes, encompassing both tectonic and non-tectonic origins [*Nikolaidis*, 2002]. Each component of the GNSS time series can be modeled as a time-dependent function to capture linear trends, periodic (seasonal) variations, coseismic and non-coseismic offsets, as well as postseismic deformation processes:

$$\begin{aligned} y(t_i) = {} & a + bt_i + c\sin(2\pi t_i) + d\cos(2\pi t_i) + e\sin(4\pi t_i) + f\cos(4\pi t_i) \\ & + \sum_{j=1}^{n_g} g_j H(t_i - \tau_g^j) + \sum_{j=1}^{n_h} h_j H(t_i - \tau_h^j) + \sum_{j=1}^{n_k} k_j H(t_i - \tau_k^j) H(\tau_k^{j+1} - t_i)\cdot t_i \\ & + \sum_{j=1}^{n_l} l_j \ln\left(1 + \frac{t_i - \tau_l^j}{m_j}\right) H(t_i - \tau_l^j) + \sum_{j=1}^{n_p} p_j \exp\left(-\frac{t_i - \tau_p^j}{r_j}\right) H(t_i - \tau_p^j) + \varepsilon_i, \end{aligned} \tag{1}$$

where t_i, $i = 1 \ldots N$ are the observation epochs, a is the initial coordinate, b is the linear velocity of station displacement, c, d, e, and f represent annual and semiannual periodic signals (e.g., seasonal, atmospheric, or oceanic tides), H is the Heaviside function. The terms g_j correspond to offsets due to equipment or software changes at time τ_g^j; h_j are coseismic offsets at time τ_h^j; k_j accounts for changes in linear velocity after earthquakes at τ_k^j. The last two summations represent postseismic transients: logarithmic (afterslip) and exponential (viscoelastic relaxation in the upper mantle and asthenosphere). ε_i denotes measurement noise.

Regression analysis is first applied to the GNSS time series to identify and remove periodic components and instrumental or tectonic offsets. Specifically, Equation 1 is initially fitted to the full time series of each station to estimate and remove seasonal signals (c, d, e, f) and instantaneous offsets (g_j, h_j), while postseismic components (l_j, p_j) are preserved in the residual series to allow the analysis of temporal variations in station velocities following earthquakes.

The resulting residual time series is then approximated by piecewise-linear splines to estimate local linear velocities b for individual time intervals. Annual intervals were selected to ensure statistical stability of the velocity estimates while maintaining sensitivity to interannual and postseismic variations. For each segment, a separate regression is performed using Equation 1 with fixed epochs τ and without re-estimating the seasonal components removed at the first stage.

The statistical reliability of the regression was assessed using the coefficient of determination (R^2) and standard errors (SE) of the estimated parameters for the linear velocities. For most stations, R^2 values ranged from 0.83 to 0.96. In Chile, horizontal velocity estimates for well-observed GNSS stations in relatively stable regions of the South American plate typically have an overall RMS error of 0.3–0.6 mm/yr, reflecting the typical precision of the measurements. Individual stations in stable regions generally show an SE of 0.2–0.5 mm/yr, whereas stations near the subduction zone, affected by coseismic jumps, postseismic transients, or data gaps, may exhibit larger uncertainties of SE = 0.7–1.0 mm/yr. Figure 2 illustrates how well the regression model fits the observed three-component GNSS time series, highlighting the accuracy of the approximation for different displacement components. Examples include a station experiencing coseismic and postseismic displacements associated with a major earthquake (ANTC, Chile) and a station located in a more stable part of the South American continent (AREQ, Peru).

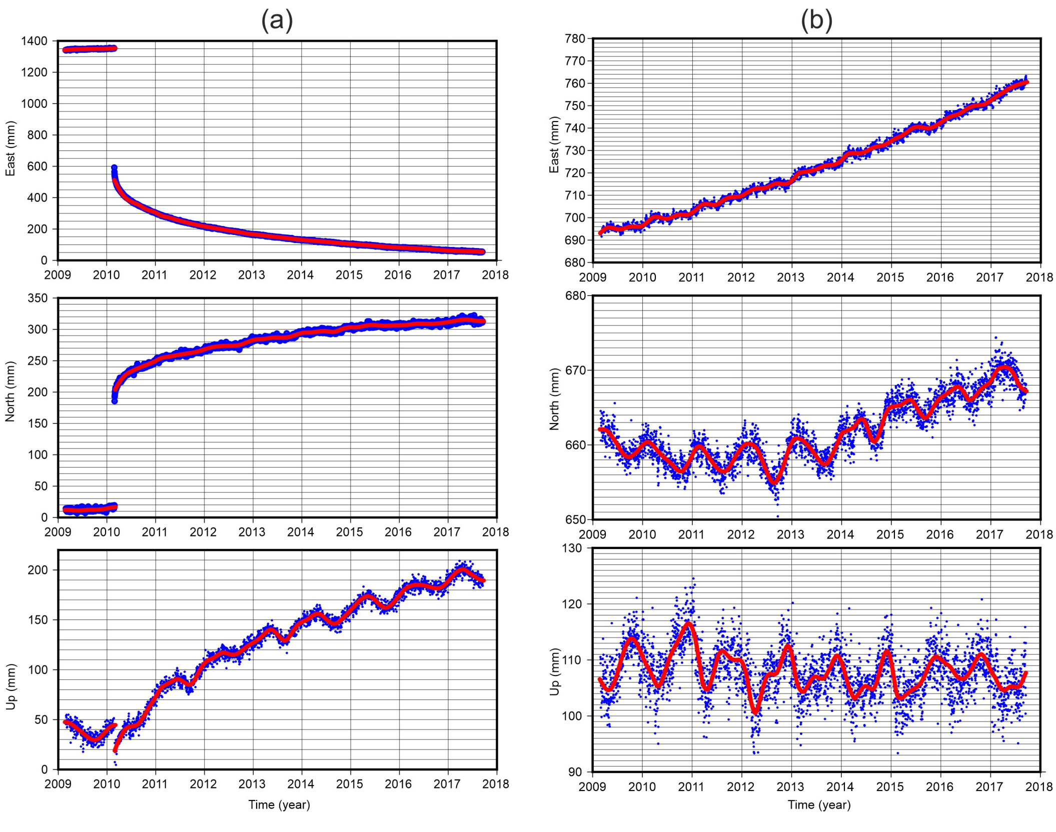

Figure 2. Three-component GNSS time series at (a) ANTC (Antuco, Chile) and (b) AREQ (Arequipa, Peru). Blue points represent the observed displacements, while the red lines show the regression model fitted to the data.

Accordingly, the input data used to estimate strain rate consist of velocity vector fields derived from GNSS observations, segmented into annual intervals covering the period from 2009 to 2017 (Figure 3), which capture both long-term tectonic motion and transient postseismic deformation in the Chilean subduction zone.

The estimation of planar strain-rate fields typically involves interpolation techniques that convert discrete GNSS velocities into a continuous deformation field. Among the widely used approaches is the method proposed by *Shen et al.* [1996]. This method provides

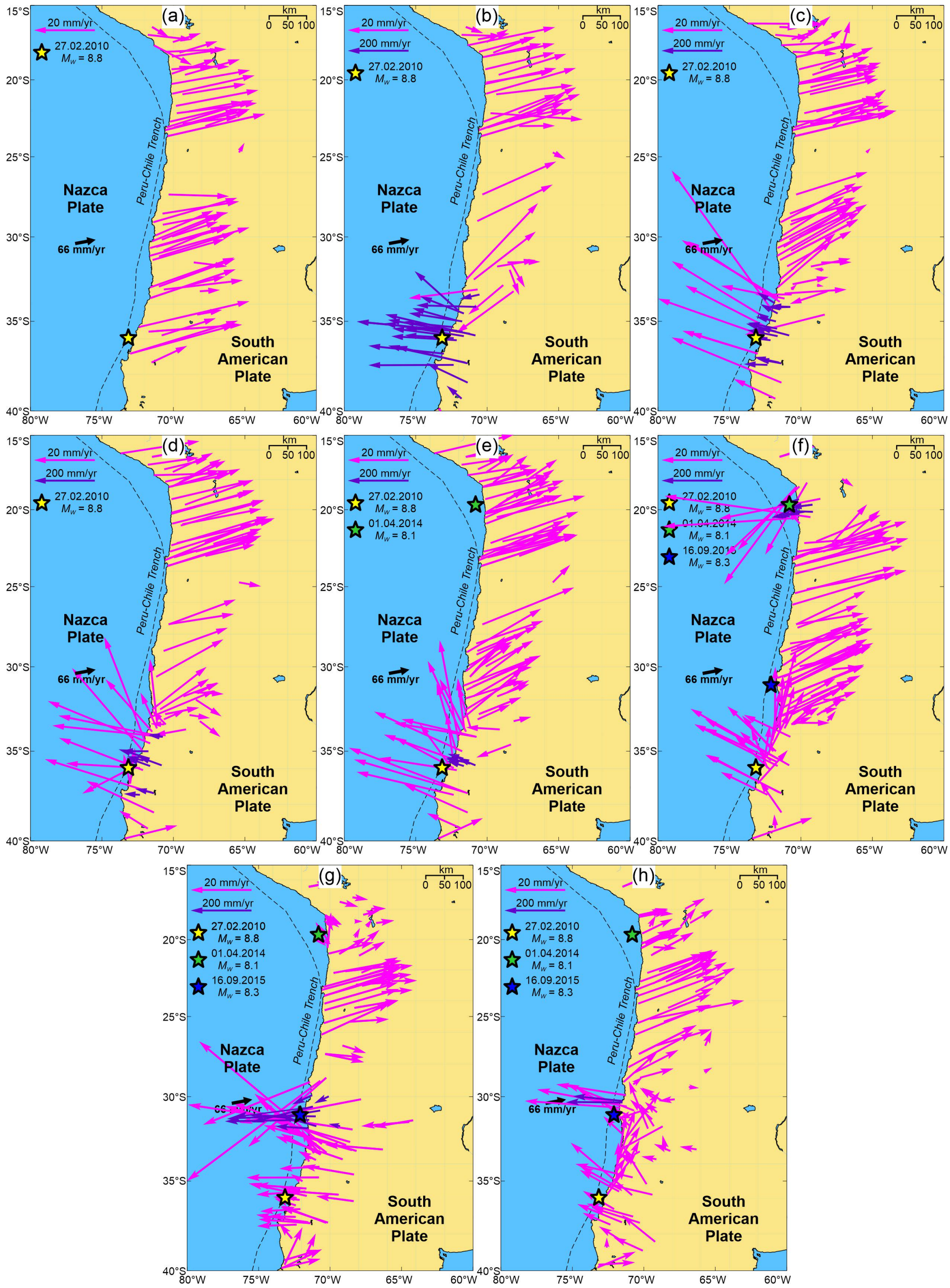

Figure 3. (a) Displacement velocities of GNSS stations with respect to stable South American plate for the periods: (a) February 27, 2009–February 26, 2010; (b) February 28, 2010–March 1, 2011; (c) March 2, 2011–March 1, 2012; (d) March 2, 2012–March 1, 2013; (e) March 2, 2013–March 31, 2014; (f) April 2, 2014–September 15, 2015; (g) September 17, 2015–September 16, 2016; (h) September 17, 2016–September 16, 2017.

a spatially continuous and smooth estimation of crustal deformation fields by fitting GNSS velocity data using a local least squares approach with distance-weighted observations. Compared to methods such as Delaunay triangulation or finite element modeling, it is computationally efficient, does not require assumptions about Earth's rheology, and allows for robust estimation of the full strain-rate tensor, including rotation and dilatation. Its flexibility in handling uneven station distribution and incorporation of measurement uncertainties make it particularly well-suited for regional tectonic analyses, including preseismic and postseismic deformation studies.

The essence of the method lies in the fact that the horizontal displacement velocity components U_x, U_y, the components of the strain-rate tensor $\dot{e}_{xx}$, $\dot{e}_{xy}$, $\dot{e}_{yy}$, and angular velocity ω at the center of a selected grid cell are related to the observed GNSS station velocities V_x^i, V_y^i by the following linear equation:

$$\begin{pmatrix} V_x^i \\ V_y^i \end{pmatrix} = \begin{bmatrix} 1 & 0 & \Delta x_i & \Delta y_i & 0 & \Delta y_i \\ 0 & 1 & 0 & \Delta x_i & \Delta y_i & -\Delta x_i \end{bmatrix} \begin{pmatrix} U_x \\ U_y \\ \dot{e}_{xx} \\ \dot{e}_{xy} \\ \dot{e}_{yy} \\ \omega \end{pmatrix} + \begin{pmatrix} \varepsilon_x^i \\ \varepsilon_y^i \end{pmatrix}. \quad (2)$$

Here, $\Delta x_i = x_i - X$ and $\Delta y_i = y_i - Y$ are the horizontal distances between the i-th GNSS station at coordinates (x_i, y_i) and the point of interest (X, Y); ε_x^i and ε_y^i are the weighted errors in the observed velocities V_x^i and V_y^i, defined as:

$$\varepsilon_x^i = \sigma_x^i \exp\left(\frac{2\Delta x_i^2}{\sigma_D^2}\right), \quad \varepsilon_y^i = \sigma_y^i \exp\left(\frac{2\Delta y_i^2}{\sigma_D^2}\right),$$

where σ_x^i and σ_y^i represent the measurement uncertainties of the respective velocity components, and σ_D is the distance decay constant (DDC). This parameter controls the smoothing radius: larger DDC values allow distant stations to have more influence, while smaller DDC values make the interpolation more localized. The value of the DDC parameter is determined based on the density and spatial distribution of GNSS stations.

The choice of the DDC constant was quantitatively justified based on the analysis of the root-mean-square error (RMSE) between observed and approximated deformation fields. RMSE is calculated as:

$$\text{RMSE} = \sqrt{\frac{1}{N}\sum_{i=1}^{N}(u_i^{\text{obs}} - u_i^{\text{model}})^2},$$

where u_i^{obs} is the observed deformation at point i, u_i^{model} is the modeled value, and N is the number of observation points. Testing DDC values from 10 to 100 km in 10 km increments for three Chilean coastal regions, with GNSS station density varying in both space and time, yielded an optimal average value of 50 km. This choice minimizes RMSE while preserving spatial detail, providing a balance between accuracy and field smoothness.

In the computation of the strain-rate components, horizontal velocity components, and rotational velocity at a given grid point, the velocity vectors from all neighboring GNSS stations located within a radius of 2 DDC are used. In this case, the coefficients ε_x^i and ε_y^i serve as weighting factors when solving the matrix Equation 2. Thus, the farther a GNSS measurement point is from the target location and the greater its associated velocity uncertainty, the smaller its contribution to the solution of the system of equations at that point. The matrix Equation 2 is solved using the least-squares method. The resulting components of the strain-rate tensor are used to derive the principal strain-rates and their corresponding orientations, as well as to identify the directions of maximum extension and shortening and the axis of maximum shear strain rate within the plane strain field. The dilatation rate and shear strain rate at each point are computed using the following expressions:

$$\Delta = \dot{e}_{xx} + \dot{e}_{yy}, \quad \Sigma = \sqrt{\left(\frac{\dot{e}_{xx} - \dot{e}_{yy}}{2}\right)^2 + \dot{e}_{xy}^2}. \quad (3)$$

We also investigated the influence of major geological structures and regional faults on the spatial distribution of strain-rate fields in the vicinity of major earthquake epicenters using a comprehensive fault database [*Maldonado et al.*, 2021].

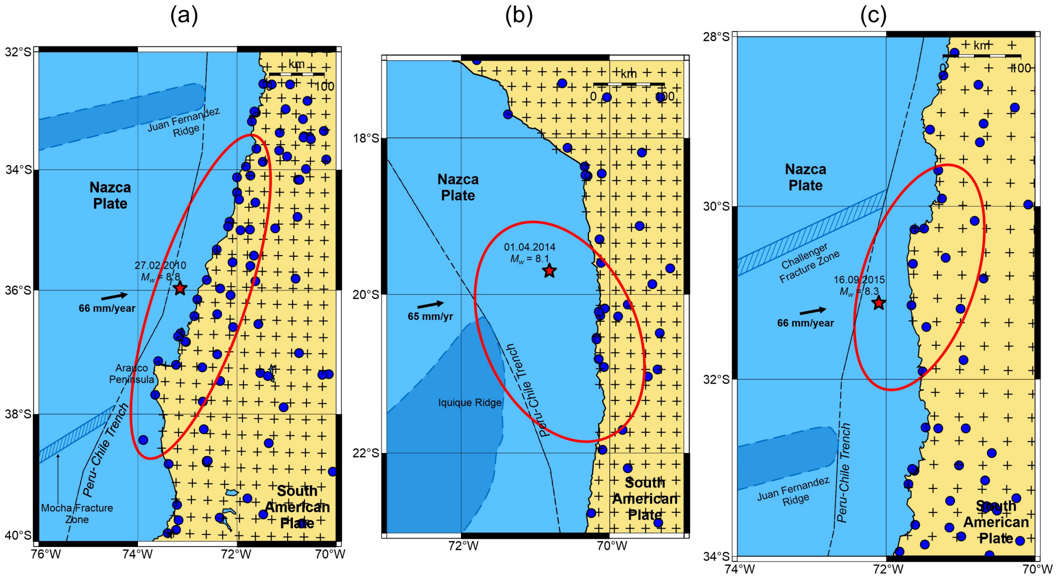

Figure 4. GNSS station locations (blue dots) and the regular grid (black crosses) used for strain calculations following the Shen method for the Maule 2010 earthquake rupture area (a), the Iquique 2014 earthquake rupture area (b), and the Illapel 2015 earthquake rupture area (c). A red ellipses in this and subsequent figures indicate the rupture zones of the Maule, Iquique, and Illapel earthquakes, defined based on the aftershock distributions and following [*Vladimirova*, 2022].

3. Crustal Deformations along the Chilean Coast Preceding and Following Major Earthquakes

To investigate the spatiotemporal evolution of crustal deformation associated with the 2010 Maule, 2014 Iquique, and 2015 Illapel earthquakes, we analyzed maps of dilatation and maximum shear strain rates over four-year time windows. For the Iquique and Illapel events, the analysis encompasses two years preceding and two years following each earthquake. In the case of the Maule earthquake, the pre-event GNSS station coverage was limited; therefore, the analysis period was adjusted to include one year prior to and three years following the mainshock. Below, we present the results of our analysis.

3.1. The 2010 Maule Earthquake

The interseismic strain field (Figures 5a and 6a) exhibits a well-defined zone of crustal contraction, with dilatation rates reaching up to -5×10^{-6} yr^{-1}, and enhanced shear strain accumulation concentrated inland of the Peru–Chile trench, particularly between ~ 36°S and 38°S. These regions spatially coincide with areas of high interplate locking (> 80%) along the megathrust, as identified in our previous study [*Vladimirova et al.*, 2025]. This spatial correlation suggests that the observed strain accumulation is driven by strong mechanical coupling at the plate interface, reflecting the buildup of tectonic stress during the interseismic period.

The early postseismic strain fields (Figures 5b and 6b), representing deformation within the first year after the 2010 Maule earthquake, reveal patterns consistent with afterslip on fault segments adjacent to the main rupture. The dilatation field (Figure 5b) shows localized extension near the northern and southern edges of the rupture (33–34°S and 37.5–38.5°S), while the central segment remains relatively undeformed. Correspondingly, the maximum shear strain field (Figure 6b) highlights enhanced shear along the boundaries of the high-slip region, as inferred from fault zone models [*Vladimirova*, 2022; *Vladimirova* *et al.*, 2025], marking areas where coseismic stress transfer likely triggered aseismic slip. These patterns align with the distribution of afterslip [*Vladimirova et al.*, 2025], concentrated on segments with relatively small coseismic slip but likely accumulated high stress during the mainshock.

During the late postseismic period (Figures 5c–d and 6c–d), the dilatation field exhibits localized extension focused along the downdip and updip margins of the main rupture zone, particularly near 33–34°S and 37.5–38.5°S. Similarly, increased maximum shear strain is observed in areas adjacent to, but largely outside, the coseismic slip region. The spatially diffuse nature of this deformation, particularly the inland extension and shear accumulation across the forearc and backarc regions, suggests that afterslip alone cannot fully account for the observed patterns. The broad zones of expansion in the dilatation field – especially landward of the rupture zone – are characteristic of vertical uplift and horizontal spreading driven by viscoelastic flow in the asthenosphere and upper mantle.

Previous studies modeling postseismic deformation following the Maule earthquake [*Bedford et al.*, 2016; *Klein et al.*, 2016] have demonstrated that incorporating a low-viscosity upper mantle layer ($\eta \approx 10^{18}$–10^{19} Pa·s) beneath the South American plate is essential to reproduce the temporal and spatial characteristics of the observed displacement fields. These models support the interpretation that viscoelastic relaxation becomes increasingly dominant in the later stages of the postseismic period, as the contribution of afterslip diminishes.

In the Maule earthquake region, regional faults (black lines) frequently coincide with zones of increased shear and dilatation, highlighting their role as key deformation boundaries or pathways for stress redistribution following megathrust slip. Their spatial alignment with strain anomalies suggests these faults underwent partial reactivation or aseismic slip during the postseismic adjustment phase.

3.2. The 2014 Iquique Earthquake

In the preseismic period, the dilatation field (Figures 7a, 7b) is dominated by slightly negative values (up to -2×10^{-6} yr^{-1}), indicating widespread crustal compression along the northern Chilean margin. The strongest contraction is concentrated near the trench and coastal forearc, consistent with elastic strain accumulation due to megathrust locking. Between two (Figure 7a) and one (Figure 7b) years before the earthquake, the overall pattern remains relatively stable, with only minor variations in the magnitude and extent of the compressional zone. This stability suggests a persistently locked interface undergoing slow elastic loading. Concurrently, the maximum shear strain-rate fields show localized concentrations of shear one year before the earthquake (Figure 8b), particularly near 20°–21.5°S, in close proximity to the eventual rupture zone. These shear anomalies correspond with the mapped faults, indicating increased shear loading in the lead-up to the earthquake. It is also worth noting that the uniform compressional pattern is consistent with the nearly homogeneous interplate locking prior to the Iquique earthquake, as inferred by *Vladimirova et al.* [2025].

Following the earthquake, the postseismic dilatation field (Figure 7c) shows a clear transition to positive values along the rupture zone and inland, indicative of horizontal extension and vertical uplift associated with stress release. This pattern is consistent with the afterslip distribution proposed by *Vladimirova et al.* [2025], which indicates that afterslip was confined to the southern portion of the rupture zone, where coseismic slip was relatively small. These results are in good agreement with the findings of *Hoffmann et al.* [2018], who extensively studied the afterslip associated with the 2014 Iquique earthquake. According to *Hoffmann et al.* [2018], afterslip accounted for a substantial portion of the total postseismic deformation, particularly during the first year following the earthquake. A similar pattern is observed in our deformation fields, which show the most significant ground displacement rates occurring in the early postseismic period. Furthermore, the spatial pattern of afterslip observed by *Hoffmann et al.* [2018] and the dilatation strain rate (Figure 7c) and maximum shear strain rate (Figure 8c) fields identified in this study

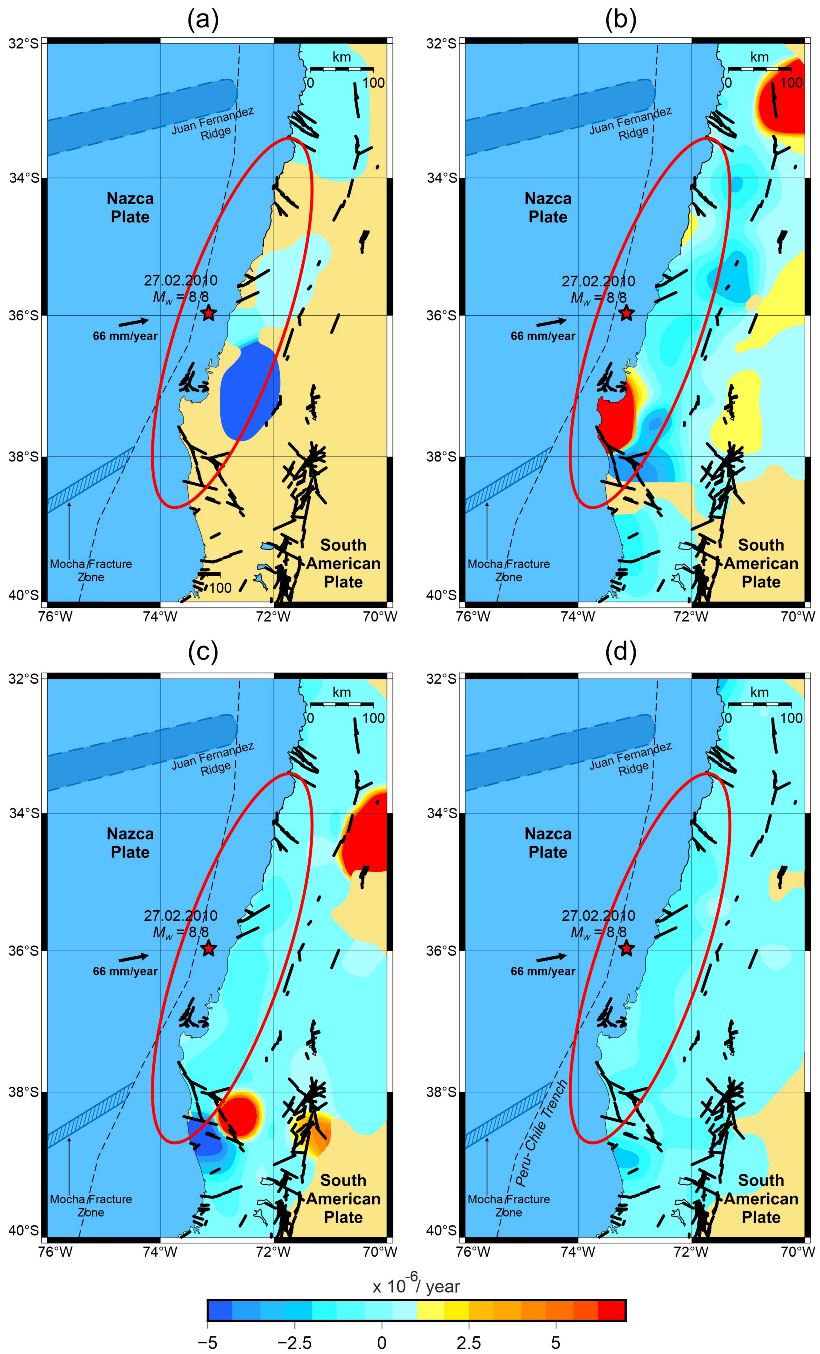

Figure 5. Spatial distribution of horizontal dilatation strain rate (in units of $\times 10^{-6}$ yr^{-1}) derived from GNSS observations for four different time windows: (a) February 27, 2009–February 26, 2010; (b) February 28, 2010–March 1, 2011; (c) March 2, 2011–March 1, 2012; (d) March 2, 2012–March 1, 2013. Negative values (blue tones) indicate horizontal contraction, while positive values (yellow to red tones) indicate horizontal extension. Red stars mark the epicenter of the 2010 Maule earthquake (M_W 8.8), and a red ellipse highlight its rupture zone. Thick black lines represent active and potentially active faults as compiled from the database [*Maldonado et al.*, 2021].

both correlate with regional fault structures. This suggests that these crustal faults play a significant role in influencing postseismic deformation, either by accommodating slip themselves or by modifying the transfer of stress within the crust. The inland migration of extension zones in the dilatation field during the later postseismic stage (Figure 7d) indicates the predominance of viscoelastic relaxation.

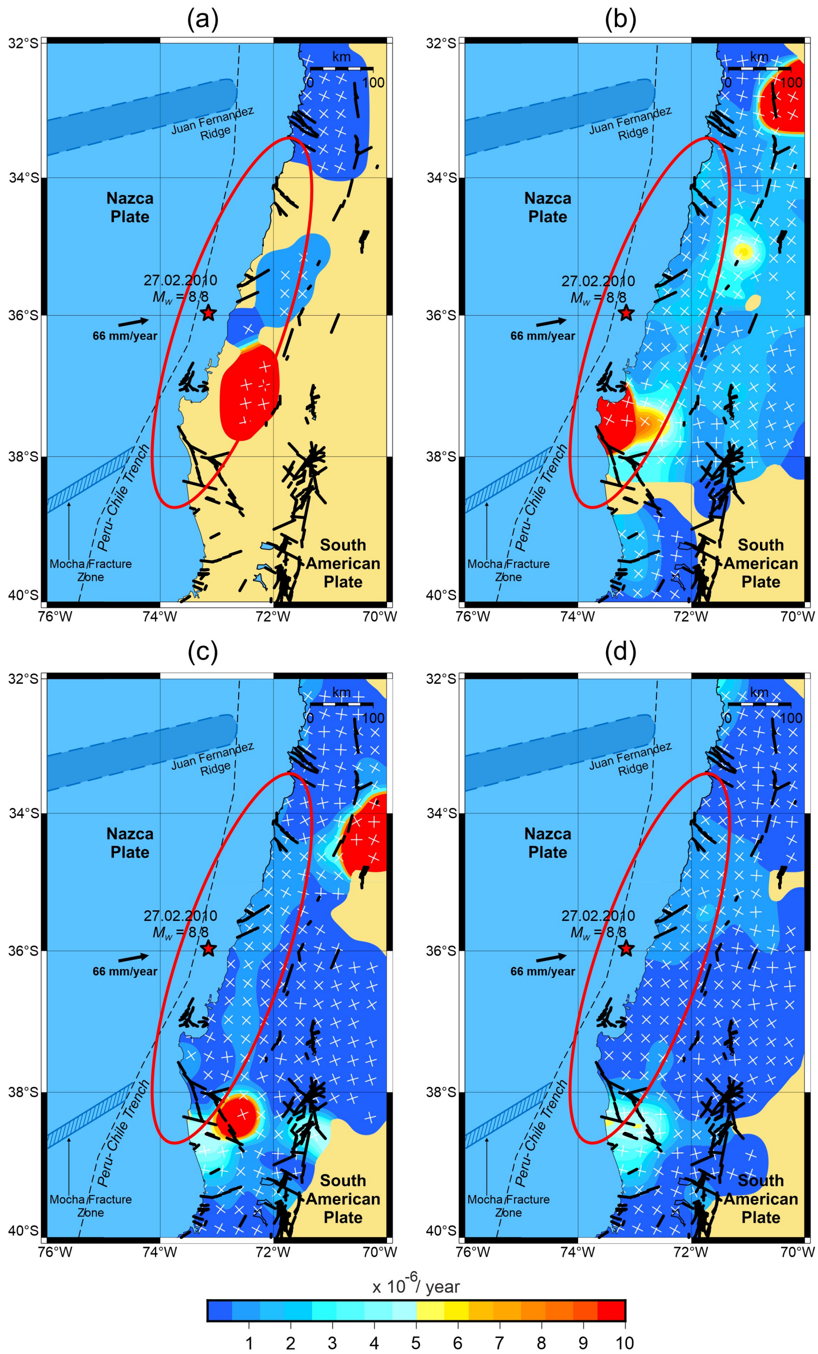

Figure 6. Spatial distribution of maximum shear strain rate (in units of $\times 10^{-6}$ yr^{-1}) for the same time windows as in Figure 5: (a) February 27, 2009–February 26, 2010; (b) February 28, 2010–March 1, 2011; (c) March 2, 2011–March 1, 2012; (d) March 2, 2012–March 1, 2013. Shear strain is shown in color scale, and overlaid white crosses indicate vector orientations of principal strain axes. Red stars mark the epicenter of the 2010 Maule earthquake (M_W 8.8), and a red ellipse highlight its rupture zone. Thick black lines represent active and potentially active faults as compiled from the database [*Maldonado et al.*, 2021].

The maximum shear strain-rate field exhibits a significant reorganization between one (Figure 8c) and two (Figure 8d) years after the earthquake: shear is significantly reduced within the central rupture zone but increases along its northern and southern margins. These changes reflect a redistribution of stress due to afterslip on adjacent segments and viscoelastic relaxation of the asthenosphere and upper mantle.

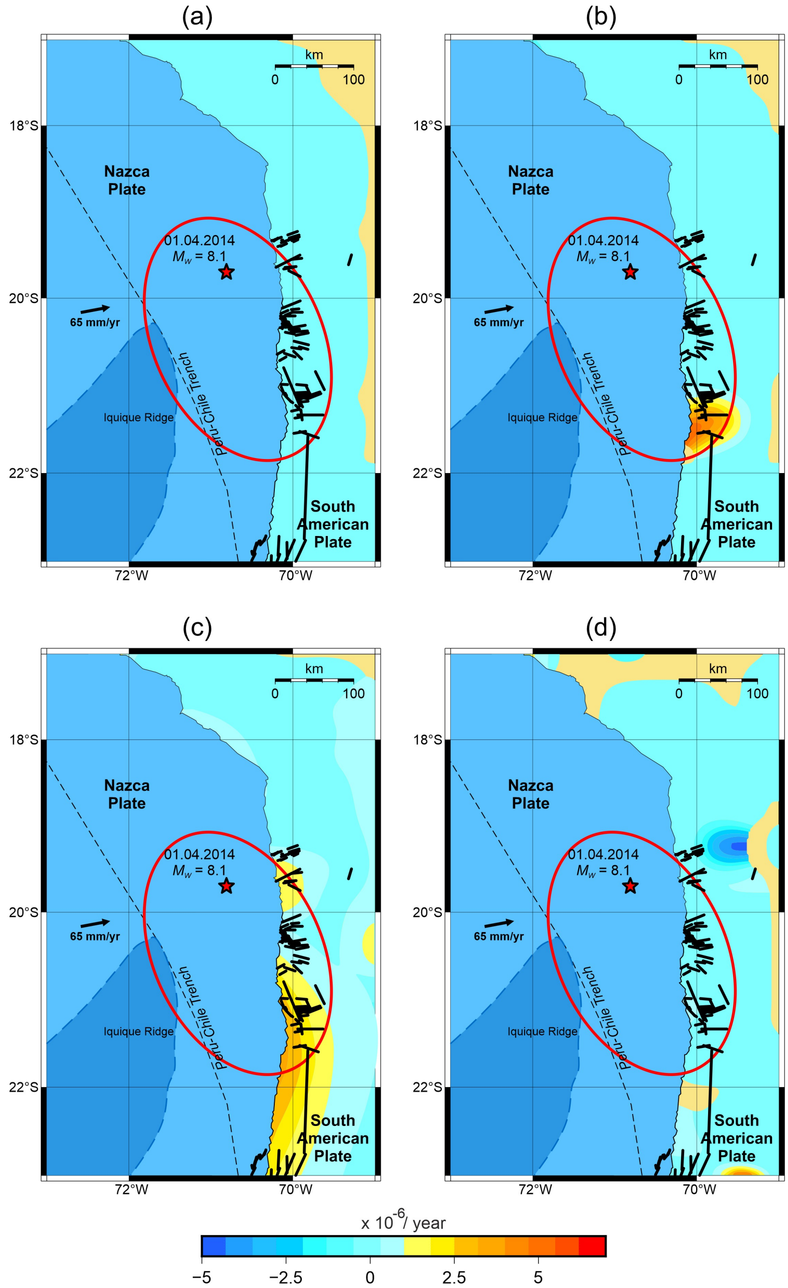

Figure 7. Spatial distribution of horizontal dilatation strain rate (in units of $\times10^{-6}$ yr^{-1}) derived from GNSS observations for four different time windows: (a) March 2, 2012–March 1, 2013; (b) March 2, 2013–March 31, 2014; (c) April 2, 2014–September 15, 2015; (d) September 17, 2015–September 16, 2016. Negative values (blue tones) indicate horizontal contraction, while positive values (yellow to red tones) indicate horizontal extension. Red stars mark the epicenter of the 2014 Iquique earthquake (M_W 8.1), and a red ellipse highlight its rupture zone. Thick black lines represent active and potentially active faults as compiled from the database [*Maldonado et al.*, 2021].

3.3. The 2015 Illapel Earthquake

During the preseismic period, the dilatation field (Figures 9a, 9b) is dominated by negative values, reaching up to -2×10^{-6} yr^{-1}, indicative of widespread horizontal compression across the central Chilean margin. Between two and one years before the earthquake, this pattern remains largely stable, suggesting that the megathrust interface was persistently locked and undergoing steady elastic loading. This pattern is supported by the interseismic coupling model, obtained in our previous study [*Vladimirova et al.*, 2025], which reveals a highly coupled segment offshore between 30° and 32°S – precisely where the coseismic rupture would later occur.

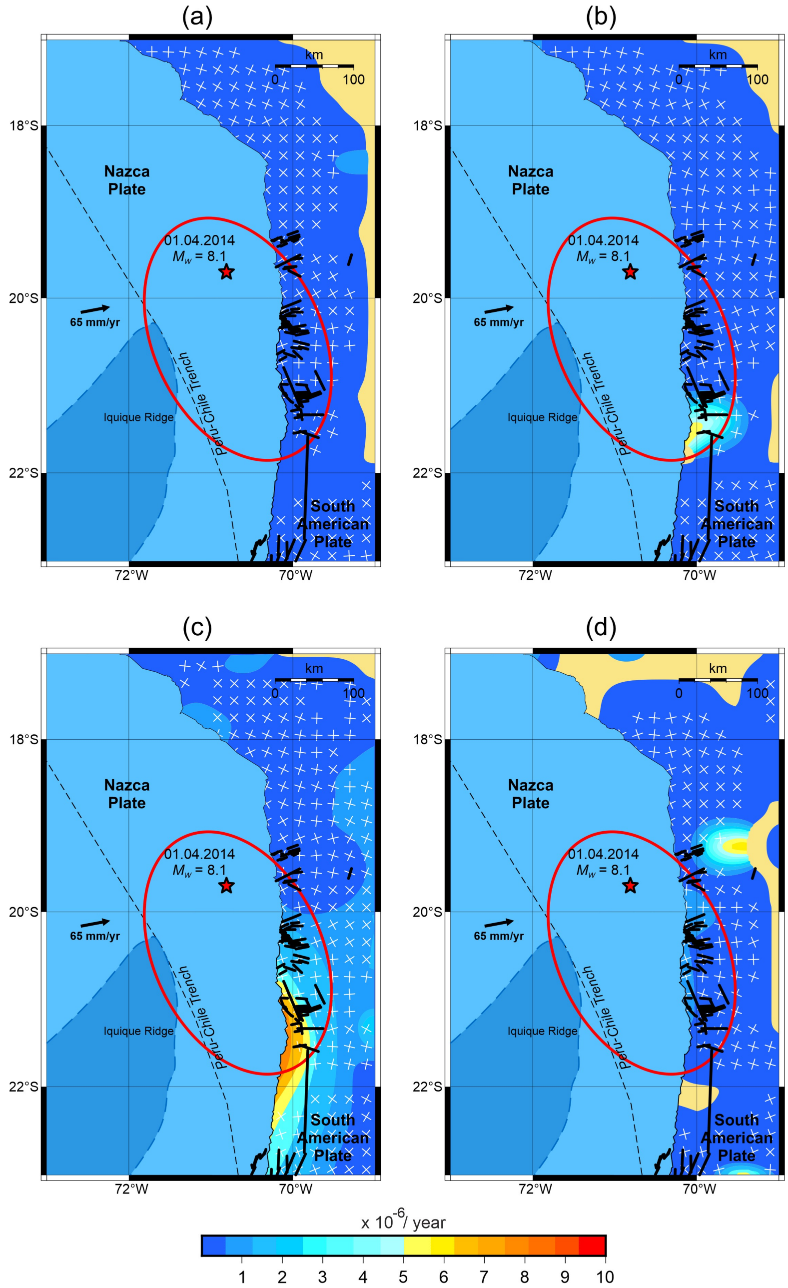

Figure 8. Spatial distribution of maximum shear strain rate (in units of $\times 10^{-6}$ yr^{-1}) for the same time windows as in Figure 7: (a) March 2, 2012–March 1, 2013; (b) March 2, 2013–March 31, 2014; (c) April 2, 2014–September 15, 2015; (d) September 17, 2015–September 16, 2016. Shear strain is shown in color scale, and overlaid white crosses indicate vector orientations of principal strain axes. Red stars mark the epicenter of the 2014 Iquique earthquake (M_W 8.1), and a red ellipse highlight its rupture zone. Thick black lines represent active and potentially active faults as compiled from the database [*Maldonado et al.*, 2021].

The positive anomaly to the east of the eventual source two years before the earthquake (Figure 9b) may reflect widespread viscoelastic relaxation following the Maule earthquake, which occurred south of the Illapel earthquake five years earlier. Simultaneously, the maximum shear strain-rate fields (Figures 10a, 10b) display low, broadly distributed values two years prior to the event with the same anomaly presumably related to the prior 2010 Maule earthquake, transitioning to another shear concentration one year before the mainshock. These shear anomalies are particularly pronounced near 32°–34°S, to the south of the eventual rupture zone. Their spatial coincidence with mapped crustal faults suggests enhanced shear loading along fault systems in the lead-up to the earthquake.

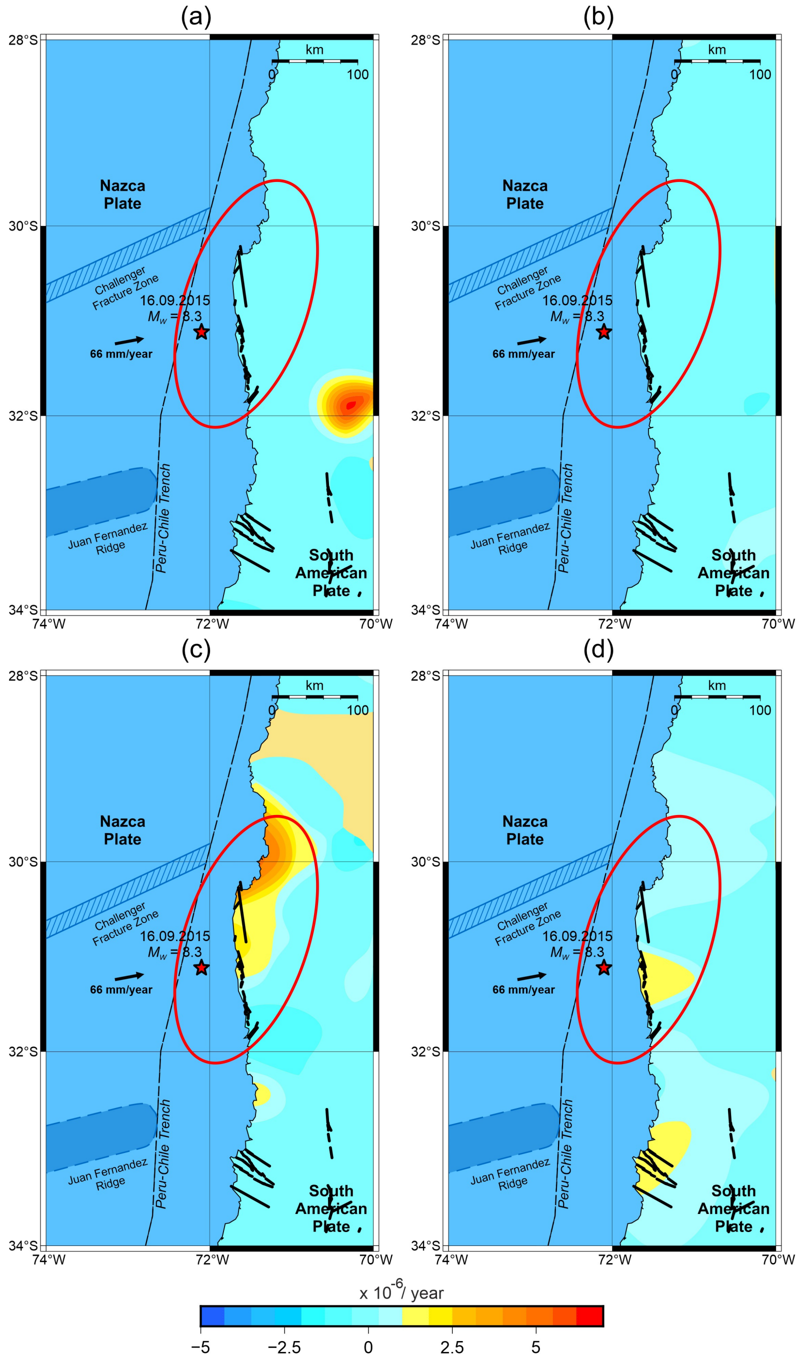

Figure 9. Spatial distribution of horizontal dilatation strain rate (in units of $\times 10^{-6}$ yr^{-1}) derived from GNSS observations for four different time windows: (a) March 2, 2013–March 31, 2014; (b) April 2, 2014–September 15, 2015; (c) September 17, 2015–September 16, 2016; (d) September 17, 2016–September 16, 2017. Negative values (blue tones) indicate horizontal contraction, while positive values (yellow to red tones) indicate horizontal extension. Red stars mark the epicenter of the 2015 Illapel earthquake (M_W 8.3), and a red ellipse highlight its rupture zone. Thick black lines represent active and potentially active faults as compiled from the database [*Maldonado et al.*, 2021].

In the postseismic phase, the dilatation field (Figures 9c, 9d) undergoes a distinct transition to positive values along the rupture zone and further inland, indicating horizontal extension and vertical uplift associated with coseismic stress release. One year after the event (Figure 9c), the highest extensional strain is stretched along almost the entire zone rupture area, consistent with afterslip occurring predominantly downdip of the coseismic slip area according to [*Vladimirova et al.*, 2025]. This pattern aligns with the early afterslip domination observed by *Shrivastava et al.* [2016] and is consistent with the spatial distribution of afterslip obtained by *Tissandier et al.* [2023]. By the second postseismic year (Figure 9d), the zones of extension migrate further inland, suggesting the increasing dominance of viscoelastic relaxation processes in the asthenosphere and upper mantle.

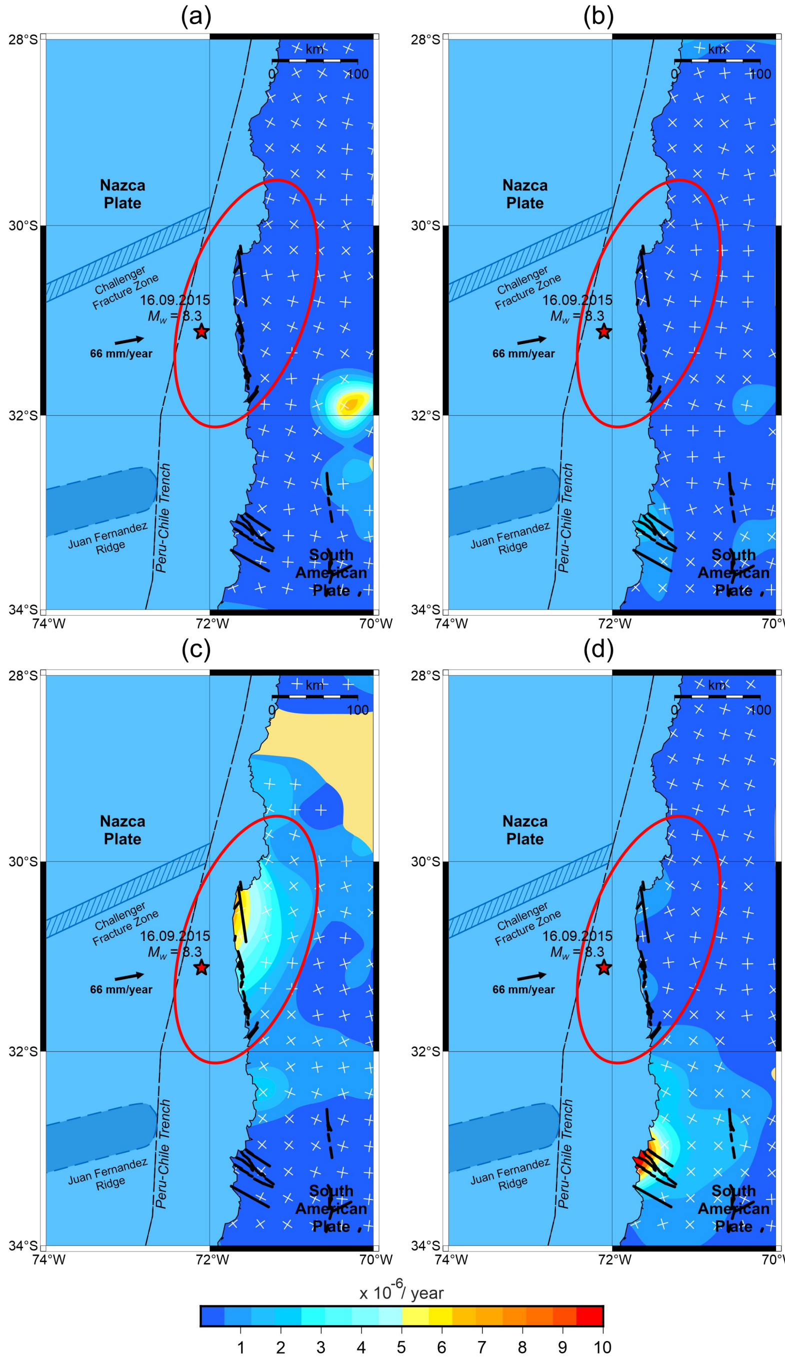

Figure 10. Spatial distribution of maximum shear strain rate (in units of $\times 10^{-6}$ yr^{-1}) for the same time windows as in Figure 9: (a) March 2, 2013–March 31, 2014; (b) April 2, 2014–September 15, 2015; (c) September 17, 2015–September 16, 2016; (d) September 17, 2016–September 16, 2017. Shear strain is shown in color scale, and overlaid white crosses indicate vector orientations of principal strain axes. Red stars mark the epicenter of the 2015 Illapel earthquake (M_W 8.3), and a red ellipse highlight its rupture zone. Thick black lines represent active and potentially active faults as compiled from the database [*Maldonado et al.*, 2021].

The maximum shear strain-rate field (Figures 10c, 10d) also exhibits substantial spatial reorganization during the postseismic stage. One year after the earthquake (Figure 10c), maximum shear strain becomes concentrated along the rupture zone of the 2015 Illapel earthquake, with pronounced accumulation in the northern segment, and noticeable extension of shear zones into the continental interior. This configuration likely reflects afterslip on adjacent fault segments and stress redistribution following the mainshock. Two years after the earthquake (Figure 10d), the central zone becomes characterized by low shear, while enhanced shear strain becomes more prominent in peripheral regions. This evolution is consistent with the combined effects of ongoing viscoelastic flow and long-term stress redistribution within the lithosphere.

Two years after the Illapel earthquake (Figure 10d), the maximum shear strain becomes increasingly localized near mapped regional crustal faults. This spatial shift suggests a progressive transfer of stress from the subduction interface to upper-plate structures, likely driven by continued viscoelastic relaxation in the asthenosphere. The alignment of high shear strain with known fault systems indicates that these faults may be reactivating or accommodating strain during the later stages of the postseismic period.

4. Discussion

Subduction zones represent inherently three-dimensional (3D) geodynamic systems characterized by complex deformation patterns along the dipping megathrust interface as well as within both the overriding and subducting lithospheric plates [*Bürgmann and Dresen*, 2008]. Despite this complexity, geodetic investigations commonly rely on two-dimensional (2D) representations of surface strain fields, including metrics such as dilatation and maximum shear strain rate, derived from horizontal velocity data obtained through GNSS or InSAR measurements [*Fialko et al.*, 2005].

The 2D strain fields employed in geodetic analyses constitute horizontal projections of the full 3D strain tensor. These fields predominantly capture lateral extensional/compressional and shear deformation at or near the Earth's surface [*Holt et al.*, 2000]. Such measurements are effective in evaluating shallow crustal deformation phenomena, including upper-plate fault activation and surface expressions of deeper processes such as viscoelastic relaxation [*Hammond et al.*, 2010]. However, these 2D fields inherently lack sensitivity to vertical deformation components and do not directly resolve strain along the inclined megathrust interface [*Schellart et al.*, 2007].

To overcome the limitations of planar strain analysis and improve the interpretation of surface strain fields in subduction zone settings, it is critical to integrate geodetic observations with geodynamic models such as afterslip, viscoelastic relaxation of the asthenosphere and upper mantle, and interseismic elastic strain accumulation along the plate boundary. Additionally, the incorporation of independent constraints – such as detailed fault mapping and structural geology – provides essential context for relating surface deformation patterns to underlying tectonic processes.

5. Conclusion

We have comprehensively analyzed the evolution of surface deformation preceding and accompanying the 2010 Maule, 2014 Iquique, and 2015 Illapel megathrust earthquakes in Chile based on GNSS-derived plane strain velocity fields. Some common patterns emerge from this analysis.

Before each earthquake, the deformation field is characterized by concentrated zones of horizontal compression and shear, consistent with a high degree of interplate locking and elastic strain accumulation along the megathrust interface. These preseismic strain anomalies are closely correlated with the location of eventual rupture areas of the corresponding megathrust earthquakes (Maule 2010, Iquique 2014, and Illapel 2015), highlighting their potential role as indicators of stress accumulation. Preseismic anomalies in the fields of maximum shear and dilatation reflect localized zones of stress concentration and mechanical weakening that precede major earthquakes. Areas of enhanced shear often delineate potential rupture pathways, while localized dilatation zones may indicate incipient fracturing or interplate interface unlocking. Together, these patterns can serve as diagnostic indicators of the evolving stress state in the crust prior to megathrust events.

The early postseismic response is dominated by afterslip, which manifests itself as localized horizontal extension and enhanced shear along the boundaries of coseismic rupture zones. In the late postseismic stages, deformation becomes more diffuse and propagates inland, consistent with viscoelastic relaxation processes in the asthenosphere and upper mantle. Notably, zones of enhanced shear and extension often coincide with mapped regional faults, indicating that these structures may be partially reactivated during postseismic relaxation or serve as stress redistribution pathways within the overriding plate.

A combined analysis of dilatation (extension) fields and maximum shear strain rates provides a robust framework for characterizing the mechanical response of the lithosphere to large megathrust earthquakes. When integrated with geodynamic modeling, these results enhance our understanding of both preseismic and postseismic deformation processes and contribute to more accurate assessments of seismic hazard in subduction zones such as the Peru–Chile margin.

Funding. This research was carried out under the state assignment of the Ministry of Science and Higher Education of the Russian Federation for the IO RAS (theme No. FMWE-2024-0018) and for the IETP RAS (No. 075-00603-25-00).

References

Beck S., Barrientos S., Kausel E., et al. Source characteristics of historic earthquakes along the central Chile subduction Askew et alzone // Journal of South American Earth Sciences. — 1998. — Vol. 11, no. 2. — P. 115–129. — https://doi.org/10.1016/s0895-9811(98)00005-4

Bedford J., Moreno M., Li S., et al. Separating rapid relocking, afterslip, and viscoelastic relaxation: An application of the postseismic straightening method to the Maule 2010 cGPS // Journal of Geophysical Research: Solid Earth. — 2016. — Vol. 121, no. 10. — P. 7618–7638. — https://doi.org/10.1002/2016jb013093

Blewitt G. W., Hammond C. and Kreemer C. Harnessing the GPS Data Explosion for Interdisciplinary Science // Eos. — 2018. — Vol. 99. — https://doi.org/10.1029/2018eo104623

Bürgmann R. and Dresen G. Rheology of the Lower Crust and Upper Mantle: Evidence from Rock Mechanics, Geodesy, and Field Observations // Annual Review of Earth and Planetary Sciences. — 2008. — Vol. 36, no. 1. — P. 531–567. — https://doi.org/10.1146/annurev.earth.36.031207.124326

Dziewonski A. M., Chou T.-A. and Woodhouse J. H. Determination of earthquake source parameters from waveform data for studies of global and regional seismicity // Journal of Geophysical Research: Solid Earth. — 1981. — Vol. 86, B4. — P. 2825–2852. — https://doi.org/10.1029/jb086ib04p02825

Easton G., González-Alfaro J., Villalobos A., et al. Complex Rupture of the 2015 Mw 8.3 Illapel Earthquake and Prehistoric Events in the Central Chile Tsunami Gap // Seismological Research Letters. — 2022. — Vol. 93, no. 3. — P. 1479–1496. — https://doi.org/10.1785/0220210283

Ekström G., Nettles M. and Dziewonski A. M. The global CMT project 2004-2010: Centroid-moment tensors for 13,017 earthquakes // Physics of the Earth and Planetary Interiors. — 2012. — Vol. 200/201. — P. 1–9. — https://doi.org/10.1016/j.pepi.2012.04.002

Fialko Y., Sandwell D., Simons M., et al. Three-dimensional deformation caused by the Bam, Iran, earthquake and the origin of shallow slip deficit // Nature. — 2005. — Vol. 435, no. 7040. — P. 295–299. — https://doi.org/10.1038/nature03425

Hammond W., Kreemer C., Blewitt G., et al. Effect of viscoelastic postseismic relaxation on estimates of interseismic crustal strain accumulation at Yucca Mountain, Nevada // Geophysical Research Letters. — 2010. — Vol. 37, no. 6. — P. L06307. — https://doi.org/10.1029/2010gl042795

Heidarzadeh M., Murotani S., Satake K., et al. Source model of the 16 September 2015 Illapel, Chile, Mw 8.4 earthquake based on teleseismic and tsunami data // Geophysical Research Letters. — 2016. — Vol. 43, no. 2. — P. 643–650. — https://doi.org/10.1002/2015gl067297

Hoffmann F., Metzger S., Moreno M., et al. Characterizing afterslip and ground displacement rate increase following the 2014 Iquique-Pisagua Mw 8.1 earthquake, Northern Chile // Journal of Geophysical Research: Solid Earth. — 2018. — Vol. 123, no. 5. — P. 4171–4192. — https://doi.org/10.1002/2017jb014970

Holt W. E., Chamot-Rooke N., Le Pichon X., et al. Velocity field in Asia inferred from Quaternary fault slip rates and Global Positioning System observations // Journal of Geophysical Research: Solid Earth. — 2000. — Vol. 105, B8. — P. 19185–19209. — https://doi.org/10.1029/2000jb900045

Kendrick E., Bevis M., Smalley B., et al. The Nazca-South America Euler vector and its rate of change // Journal of South American Earth Sciences. — 2003. — Vol. 16, no. 2. — P. 125–131. — https://doi.org/10.1016/s0895-9811(03)00028-2

Klein E., Fleitout L., Vigny C., et al. Afterslip and viscoelastic relaxation model inferred from the large-scale post-seismic deformation following the 2010 Mw 8.8 Maule earthquake (Chile) // Geophysical Journal International. — 2016. — Vol. 205, no. 3. — P. 1455–1472. — https://doi.org/10.1093/gji/ggw086

Lay T., Yue H., Brodsky E. E., et al. The 1 April 2014 Iquique, Chile, Mw 8.1 earthquake rupture sequence // Geophysical Research Letters. — 2014. — Vol. 41, no. 11. — P. 3818–3825. — https://doi.org/10.1002/2014gl060238

Lin Y. N., Sladen A., Ortega-Culaciati F., et al. Coseismic and postseismic slip associated with the 2010 Maule Earthquake, Chile: Characterizing the Arauco Peninsula barrier effect // Journal of Geophysical Research: Solid Earth. — 2013. — Vol. 118, no. 6. — P. 3142–3159. — https://doi.org/10.1002/jgrb.50207

Maldonado V., Contreras M. and Melnick D. A comprehensive database of active and potentially-active continental faults in Chile at 1:25,000 scale // Scientific Data. — 2021. — Vol. 8, no. 1. — https://doi.org/10.1038/s41597-021-00802-4

Métois M., Vigny C. and Socquet A. Interseismic Coupling, Megathrust Earthquakes and Seismic Swarms Along the Chilean Subduction Zone (38°–18°S) // Pure and Applied Geophysics. — 2016. — Vol. 173, no. 5. — P. 1431–1449. — https://doi.org/10.1007/s00024-016-1280-5

Mikhailov V. O., Timoshkina E. P., Smirnov V. B., et al. On the Origin of Postseismic Deformation Processes in the Region of the Maule, Chile Earthquake of February 27, 2010 // Izvestiya, Physics of the Solid Earth. — 2020. — Vol. 56, no. 6. — P. 762–771. — https://doi.org/10.1134/s106935132006004x

Mora-Stock C. and Rabbel W. Maule Mw 8.8 earthquake: a seismological review // The Chilean Earthquake and Tsunami 2010. — Boston : WIT Press, 2012. — P. 1–24. — https://doi.org/10.2495/978-1-84564-670-7/01

Moreno M., Rosenau M. and Oncken O. 2010 Maule earthquake slip correlates with pre-seismic locking of Andean subduction zone // Nature. — 2010. — Vol. 467, no. 7312. — P. 198–202. — https://doi.org/10.1038/nature09349

Nikolaidis R. Observation of Geodetic and Seismic Deformation with the Global Positioning System : PhD thesis / Nikolaidis R. — San Diego : University of California, 2002. — 305 p.

Ruiz S., Metois M., Fuenzalida A., et al. Intense foreshocks and a slow slip event preceded the 2014 Iquique Mw 8.1 earthquake // Science. — 2014. — Vol. 345, no. 6201. — P. 1165–1169. — https://doi.org/10.1126/science.1256074

Ruiz S. A. and Madariaga R. Historical and recent large megathrust earthquakes in Chile // Tectonophysics. — 2018. — Vol. 733. — P. 37–56. — https://doi.org/10.1016/j.tecto.2018.01.015

Schellart W. P., Freeman J., Stegman D. R., et al. Evolution and diversity of subduction zones controlled by slab width // Nature. — 2007. — Vol. 446, no. 7133. — P. 308–311. — https://doi.org/10.1038/nature05615

Shen Z., Jackson D. and Ge B. Crustal deformation across and beyond the Los Angeles basin from geodetic measurements // Journal of Geophysical Research: Solid Earth. — 1996. — Vol. 101, B12. — P. 27957–27980. — https://doi.org/10.1029/96JB02544

Shrivastava M. N., González G., Moreno M., et al. Coseismic slip and afterslip of the 2015 Mw 8.3 Illapel (Chile) earthquake determined from continuous GPS data // Geophysical Research Letters. — 2016. — Vol. 43, no. 20. — https://doi.org/10.1002/2016gl070684

Tissandier R., Nocquet J.-M., Klein E., et al. Afterslip of the Mw 8.3 2015 Illapel earthquake imaged through a time-dependent inversion of continuous and survey GNSS data // Journal of Geophysical Research: Solid Earth. — 2023. — Vol. 128, no. 2. — https://doi.org/10.1029/2022jb024778

Vladimirova I. S. Study of the Features of Seismogenic Activation of the Chilean Subduction Zone at the Beginning of the 21st Century // Doklady Earth Sciences. — 2022. — Vol. 507, no. 2. — P. 1112–1117. — https://doi.org/10.1134/s1028334x22600943

Vladimirova I. S., Gabsatarov Y. V. and Shcheveva N. S. A Series of Strong Earthquakes in Chile at the Beginning of the 21st Century: Similarities, Differences, Relationship // Russian Journal of Earth Sciences. — 2025. — ES2013. — https://doi.org/10.2205/2025es000972